An Efficient Discovery of Active, Selective and Stable Catalysts for Electrochemical H_2O_2 Synthesis through Active Motif Screening

Seoin Back,[*,†,§] Jonggeol Na,[‡,§] and Zachary W. Ulissi[*,¶]

†Department of Chemical and Biomolecular Engineering, Institute of Emergent Materials, Sogang University, Seoul, 04107, Republic of Korea

‡Division of Chemical Engineering and Materials Science, Ewha Womans University, Seoul 03760, Republic of Korea

¶Department of Chemical Engineering, Carnegie Mellon University, Pittsburgh, Pennsylvania 15217, United States

§These authors contributed equally to this work.

E-mail: sback@sogang.ac.kr; zulissi@andrew.cmu.edu

Abstract

Electrochemical reduction of O_2 provides a clean and decentralized pathway to produce H_2O_2 compared to the current energy-intensive anthraquinone process. As the electrochemical reduction of O_2 proceeds via either two-electron or four-electron pathway, it is thus essential to control the selectivity as well as to maximize the catalytic activity. Siahrostami et al. demonstrated a novel approach to control the reaction pathway by optimizing an adsorption ensemble to tune adsorption sites of reaction intermediates, and identified Pt-Hg catalysts from density functional theory (DFT) calculations and experimentally validated this catalyst (*Nat. Mater. 2013, 12, 1137*). Inspired by this concept, in this work, we apply a state-of-the-art high-throughput screening to develop O_2 reduction catalyst for selective H_2O_2 production. Starting from Materials Project database, we evaluate activity, selectivity and electrochemical stability. To efficiently perform the screening, we introduce an active motif based approach which pre-screens unpromising materials and only performs DFT calculations for promising materials, which significantly reduce the number of the required calculations. We not only provide a list of promising candidates identified by DFT calculations, but also suggest element species to achieve high catalytic activity or H_2O_2 selectivity for future experimental attempts. Finally, we discuss a strategy for efficient future high-throughput screening using a machine learning pipeline consisting of a non-linear dimension reduction and a density-based clustering.

Keywords

Density Functional Theory Calculations, High-throughput Screening, Hydrogen Peroxide, Intermetallic Alloys, Active Motif Screening, Ensemble Effect, Ligand Effect
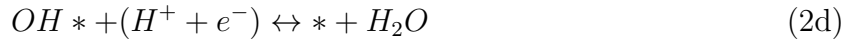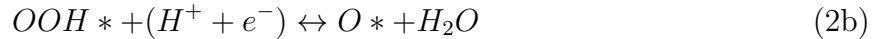
1. Introduction

A direct production of hydrogen peroxide (H_2O_2) through an electrochemical oxygen ($/rmO_2$) reduction reaction (ORR) under ambient conditions is a desirable pathway to replace energy-intensive and centralized anthraquinone process.[1] Further, this process can resolve an energy storage issue of intermittent renewable energy sources such as solar or wind power, by storing renewable-source-derived electricity as chemical bonding energies of the liquid fuel.[2] The produced H_2O_2 could also be utilized in paper industry and water treatment.[3] Several types of electrocatalysts have been reported so far, including intermetallic alloys ($PtHg_4$,[4] Pd_2Hg_5[5]), defective/oxidized carbon-based materials,[6–9] and single atom catalysts.[10,11]

Two-electron pathway ($E^{\circ}_{O_2/H_2O_2}$=0.7 V_{RHE}):

$$* + O_2 + (H^+ + e^-) \leftrightarrow OOH* \tag{1a}$$

$$OOH * + (H^+ + e^-) \leftrightarrow * + H_2O_2 \tag{1b}$$
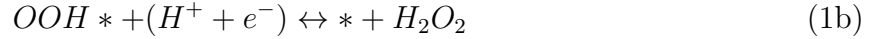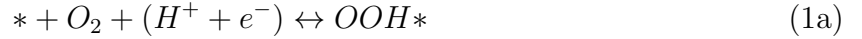
Four-electron pathway ($E^{\circ}_{O_2/H_2O}$=1.23 V_{RHE}):

$$* + O_2 + (H^+ + e^-) \leftrightarrow OOH* \tag{2a}$$

$$OOH * + (H^+ + e^-) \leftrightarrow O * + H_2O \tag{2b}$$

$$O * + (H^+ + e^-) \leftrightarrow OH* \tag{2c}$$

$$OH * + (H^+ + e^-) \leftrightarrow * + H_2O \tag{2d}$$

The electrochemical O_2 reduction could follow two different pathways depending on the properties of catalyst surfaces, *i.e.,* two- ((1a) and (1b)) and four-electron ((2a)-(2d)) pathways to produce H_2O_2 and H_2O, respectively. Thus, improving the product selectivity toward H_2O_2 is of significant importance as well as maximizing the catalytic activity. As shown in Eqn (1a) and (2a), two- and four-electron pathways share the initial step, the protonation

of O_2 to make OOH* on the surface, and the following protonation of OOH* determines the product selectivity. Thus, to enhance the product selectivity for H_2O_2, adsorbed O* should be destabilized, so that H_2O_2 formation becomes energetically more favorable (Figure 1A), assuming that a kinetic barrier of a proton transfer from H_3O^+ (acid) or H_2O (base) to adsorbate is proportional to the reaction energy.[12] However, binding strength of ORR intermediates (O*, OH*, OOH*) is correlated with each other on catalyst surfaces through so-called "scaling relation", making it challenging to control the binding strength of adsorbates independently.[13–16]

Toward a rational catalyst design, Siahrostami et al. suggested that an ensemble effect, *i.e.,* arrangements of surface atoms to change adsorption sites of reaction intermediates, is the key to control the product selectivity.[4] For example, O* adsorbate generally prefers to adsorb at the face centered cubic (FCC) hollow site of FCC metal [111] surfaces, interacting with three surface metal atoms (Figure 1B). In the case of $PtHg_4$ intermetallic alloy surface found to be selective for H_2O_2 production,[4] however, surface Pt atom is surrounded by four inactive Hg atoms removing the Pt-Pt-Pt active motif and substantially weakening O* adsorption by changing the adsorption site to the top site. On the other hand, the adsorption site and energy of OOH* remained nearly unchanged, thus making $PtHg_4$ very active and selective toward H_2O_2 production (Figure 1B). To the best of our knowledge, however, there has been no attempt to systematically discover active, selective and stable catalysts from large materials databases, mainly due to the difficulty of modelling many possible surfaces and active sites, and computational cost of performing DFT calculations for all those sites.

In this work, we present an active motif screening from the materials database to discover catalysts that outperform the state-of-the-art catalysts in multiple aspects. We first performed the conventional DFT calculations to compare binding affinities of diverse elements in the periodic table toward O-species to determine promising bimetallic combinations. We then screened materials based on the stability under the reaction conditions, and the active motif to maximize the catalytic activity and H_2O_2 selectivity simultaneously. We also per-

formed general non-linear dimension reduction and density-based clustering to increase the interpretability of fingerprint, which leads to accelerated inverse catalysts design. This work highlights that the active motif screening could significantly reduce the number of DFT calculations to accelerate catalysts discovery, and this approach could also be applied to other catalytic reactions requiring new materials that deviate from the conventional scaling relations.

2. Computational Details

We performed DFT calculations using VASP code (version 5.4.4.)[17,18] with GGA-RPBE[19] exchange-correlation functional and projector augmented wave (PAW) pseudopotentials[20] with a cutoff energy of 400 eV. Energy and force criteria for the convergence were set to 10^{-4} eV and 0.05 eV/Å, respectively. We modeled Ag-based single atom alloys using 3-layered (3×3) supercell of [111] facet (9 atoms in each layer), and one surface Ag atom was replaced by other elements, which include 22 p-block and 29 d-block elements (Table S1). ($2 \times 2 \times 1$) Monkhorst-pack meshes were used for all single atom alloy calculations. For high-throughput intermetallic surface calculations, we determined the k-points ($k_1 \times k_2 \times 1$) so that $a_n \times k_n (n = 1, 2) \approx 15$ Å, where a_1 and a_2 are the sizes of unit vectors in x and y directions, respectively. For all surface structures, a vacuum of at least 12 Å was included to avoid an imaginary interaction along the z-axis.

To establish the free energy diagram of electrochemical O_2 reduction to H_2O_2, we first calculated electronic energies of bare and O*/OOH* adsorbed surfaces. Free energy corrections for adsorbates (zero-point energies, enthalpic and entropic contributions) were then determined based on the harmonic oscillator approximation at 300 K on Pt [111] surface. For H_2O and H_2 molecules, we calculated free energy corrections using the ideal gas approximation implemented in ASE[21] at 3,534 Pa and 101,325 Pa of their partial pressures, respectively (Table S2). We further added the solvation stabilization of -0.25 eV for OOH*

assuming a half-dissociated water layer.[22] To take into account the effect of the electrode potential, we used the computational hydrogen electrode (CHE) method,[23] which assumes an equivalent chemical potential of a half of H_2 gaseous molecule and proton-electron pair, *i.e.*, $G(H^+ + e^-) = 0.5G(H_2)$ at standard conditions (pH=0, and P_{H_2}=101,325 Pa) in the absence of the applied potential. Once the potential U is applied, $G(H^+ + e^-) = 0.5G(H_2) - eU_{elec}$, where e is an elementary charge of an electron and U is the electrode potential versus reversible hydrogen electrode (RHE), thus enabling to calculate the potential dependent free energies along the reaction pathway and to estimate theoretical overpotentials for H_2O_2 production ($\eta_{H_2O_2}$).
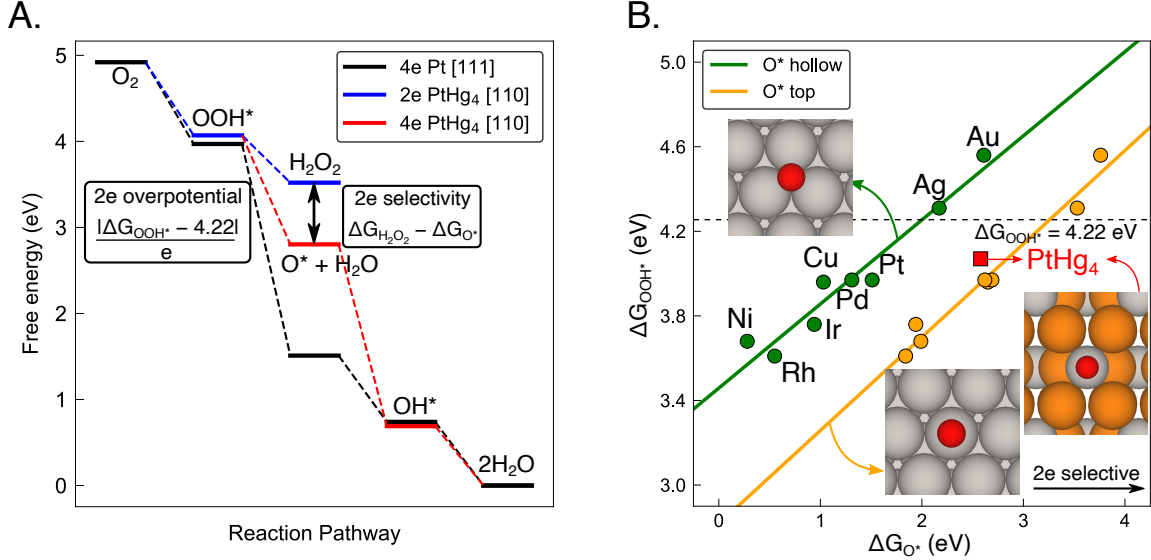
3. Results and discussions

Figure 1: (A) Free energy diagram of ORR on Pt [111] and PtHg$_4$ [110] at 0 V$_{RHE}$. For PtHg$_4$, we plotted 2e and 4e reaction pathways to produce H$_2$O$_2$ and H_2O, denoted as blue and red lines, respectively. 2e overpotential and selectivity are defined, which will be used throughout the rest of the paper. (B) Scaling relation between ΔG_{OOH*} and ΔG_{O*} of pure metal [111] surfaces. Green and orange lines indicate hollow and top site binding for O* adsorption, respectively. Inset images are top views of O* adsorptions. Note that ΔG_{O*} on PtHg$_4$ is located close to the scaling line of top site O* binding. Color codes in atomic structures: Pt (grey), Hg (orange), O (red). ΔG_{OOH*} value to achieve the best catalytic activity is presented with the dashed horizontal line. For higher H$_2$O$_2$ selectivity as highlighted with the arrow, weaker ΔG_{O*} is preferred.

Figure 1A compares free energies of ORR on the transition metal catalyst, Pt [111], and the intermetallic catalyst, PtHg$_4$ [110]. The scaling relation generally predicts similar binding strength of OOH* when O* binding is similar.[16] However, ΔG_{O*} on PtHg$_4$ (2.87 eV) is much weaker than Pt (1.51 eV) by ~1.3 eV, although their ΔG_{OOH*} are very similar, making PtHg$_4$ exceptionally selective for the 2e reaction pathway.[4] To understand the origin of such difference, we plotted projected density of states (pDOS) and calculated d-band center (Figure S1) of Pt [111] and PtHg$_4$ [110] surfaces, which is a descriptor for binding affinity toward adsorbates.[24] Very close d-band center values and similar binding energies at the top site of OOH* for Pt [111] and PtHg$_4$ [110] indicate that the electronic effect could

barely affect the product selectivity between two catalysts. We compared O* binding at the single-fold top site and many-fold sites on the two surfaces. O* binding obviously preferred many-fold sites consisting of O-affinitive surface Pt atoms for Pt [111] surface, while the top site is most preferred for $PtHg_4$ [110] surface (Figure S1). This suggests that the change in the binding sites due to the ensemble effect, where Pt site is isolated by surrounding Hg atoms, could mainly contribute to the enhanced H_2O_2 selectivity of $PtHg_4$. In Figure 1B, we plotted the scaling relation between ΔG_{OOH*} and ΔG_{O*}, where two different O* binding sites were considered (Figure 1B inset). Interestingly, the top site O* binding on the transition metals is ~1.3 eV weaker in average compared to the hollow site binding. This observation confirms that O* binding became selectively weaker on $PtHg_4$ as the hollow site disappeared (Figure S1), and highlights the potential of the active motif engineering for selective catalysis by escaping from the conventional scaling relations.

The active motif engineering can be achieved through alloying two or more elements. However, it is very challenging to find the ideal catalysts through the conventional computational screening, which enumerates surfaces, finds unique active sites for all possible crystal structures and element combinations, and perform DFT calculations. For example, 1,499 intermetallic crystal structures resulted in 17,507 unique surfaces and 1,684,908 unique binding sites,[25] requiring new methods to reduce the number of DFT calculations. To resolve this computational cost issue, many machine learning approaches have been reported including fingerprint-based artificial neural network,[25] graph-based convolutional neural network,[26,27] data-driven automatic machine learning,[28] but all those approaches require sufficient training DFT calculations to guarantee reasonable prediction accuracy. In the following, we discuss our approach to tackle this challenge in discovering new 2e ORR catalysts through the active motif screening.

Filtering Criteria for Bulk Materials

In intermetallic alloys, not only crystal structures but also constituting elements are important. For example, alloying two oxygen affinitive elements is not suitable for the selective destabilization of O* to achieve high H_2O_2 selectivity, since it cannot remove the most stable O* hollow sites. Thus, to effectively remove three (or higher)-fold hollow active motifs for O* binding on, combinations of strong and weak O-binding elements are desirable as in $PtHg_4$. To determine suitable element combinations, we first compared oxygen binding strength of elements in the same local environment by constructing Ag-based single metal alloy systems, where one surface Ag atom is replaced by other elements (51 elements) in (3×3) Ag [111] surface (Figure S2). We calculated ΔG_{OH*} on the single atom alloys and identified active and inactive elements toward O-species based on ΔG_{OH*}. We collected elements with ΔG_{OH*} weaker than 0.75 eV, the typical value of Pt [111] surface, resulting in 12 elements (Ag, Au, Hg, S, Tl, Se, Br, C, Cl, F, I, N) (Table S1). Interestingly, Hg binds OH* most weakly among all elements considered, accounting for the success of $PtHg_4$ and Pd_2Hg_5 catalysts.[4,5]

Figure 2 shows the procedure of bulk material filtering based on various criteria. We first collected all bulk materials across 48 elements (see the periodic table in Figure 2) from Materials Project[29] (11,476), and only considered binary alloys for simplicity (3,568). We note that an electrochemical stability ($\Delta G_{\text{Pourbaix}}$) under the reaction conditions (pH and V) is one of the most important factors for electrocatalysts, which has barely been investigated in literature.[30–32] Using the Pourbaix analysis module,[29] we calculated $\Delta G_{\text{Pourbaix}}$ of catalysts at the reaction conditions with three different pHs, that is, U (V) = $0.7 - 0.0591 \times$pH (pH=0, 7, 14). We note that acid-stability is mainly discussed in this paper, but stabilities under different conditions can be found in Supporting Information. We only collected materials with $\Delta G_{\text{Pourbaix}}$ less than 1.0 eV/atom with respect to the most stable phases of the combinations assuming materials' metastability and uncertainty of the approach. We note that $\Delta G_{\text{Pourbaix}}$ of experimentally acid-stable $PtHg_4$ and Pd_2Hg_5 were calculated to be 0.19 and
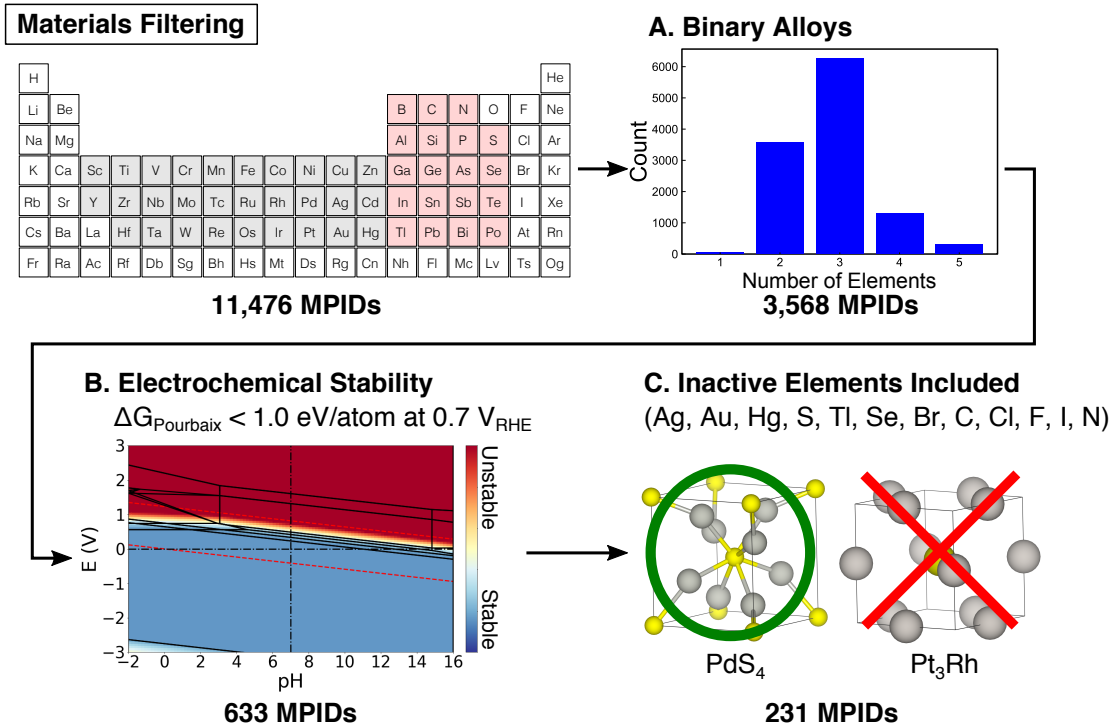
Figure 2: Criteria to filter bulk materials from Materials Project.[29] Considered *p*-block and *d*-block elements are highlighted as pink and grey shaded box, respectively. (A) We considered only binary alloys for simplicity. (B) The electrochemical stability was evaluated and materials with the stability higher than 1.0 eV/atom above the hull were removed. (C) We chose materials consisting of active and inactive elements, which were identified by DFT calculations on the single atom alloys (Table S1).

0.26 eV/atom, respectively, at pH=0 and 0.7 V. Even rather loose stability condition filtered out more than 80 % of the materials considered, highlighting the importance of considering the electrochemical stability at the reaction conditions to reduce the number of unnecessary DFT calculations that are considerably unstable under the experimental conditions. Finally, we collected materials consisting of active and inactive elements, reducing the number of materials to 231.

Filtering Criteria for Surface Structures

Using 231 materials, we enumerated various unique low index slab structures ([1,0,0], [0,1,0], [0,0,1], [1,1,0], [0,1,1], [1,0,1], [1,1,1]) and identified all unique active sites in each slab struc-
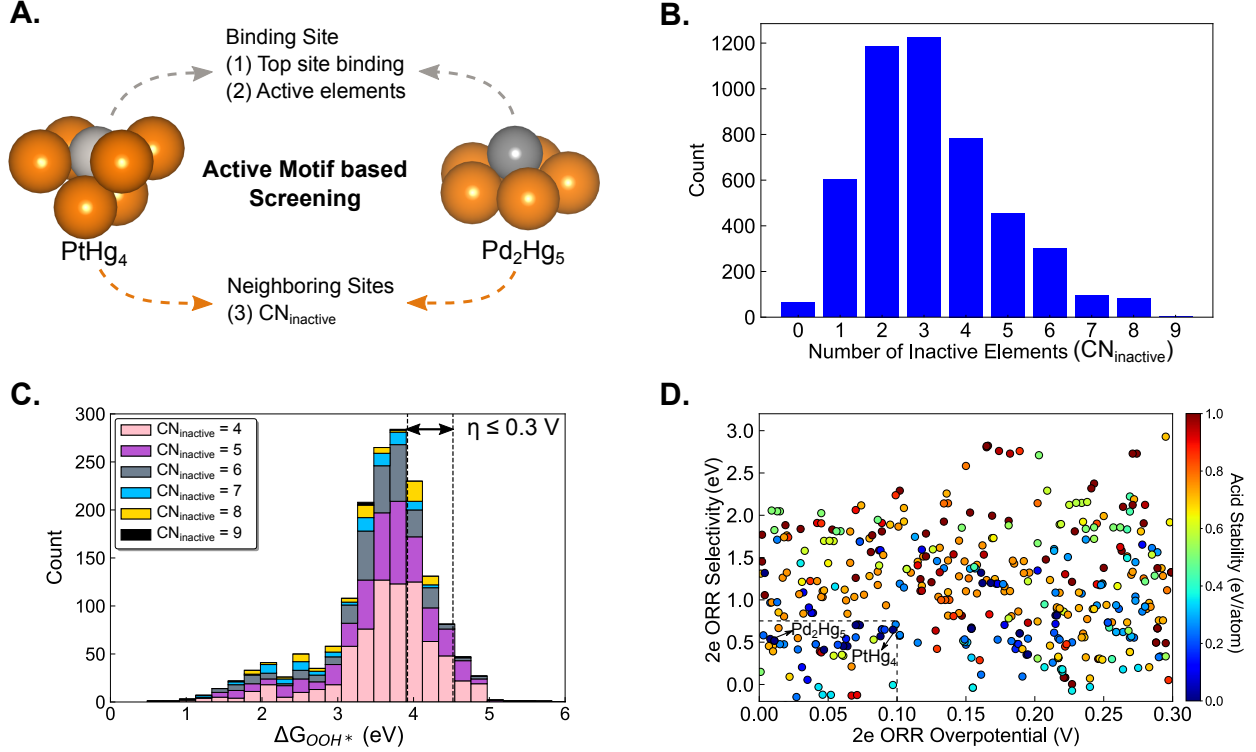
Figure 3: (A) Filtering criteria to effectively select active and selective motifs for H_2O_2 production. Tilted views of $PtHg_4$ and Pd_2Hg_5 with their active motifs (light (Pt) and dark (Pd) grey) and the first nearest neighbors (orange (Hg)) are shown as examples. (B) A histogram of structures with different numbers of inactive elements surrounding the active sites. (C) A histogram of ΔG_{OOH*} with colors indicating $CN_{inactive}$. Vertical dashed lines denote a range to achieve overpotentials of 0.3 V or less ($3.92 \leq \Delta G_{OOH*} \leq 4.52$). (D) 2e ORR selectivity is plotted versus 2e ORR overpotential. 2e ORR selectivity is calculated as $\Delta G_{H_2O_2} - \Delta G_{O*}$. The lower in y-direction, the more selective toward the target product, H_2O_2. Thus, catalysts close to the bottom left corner are expected to be active and selective. Marker colors correspond to their acid-stability. $PtHg_4$ and Pd_2Hg_5 are plotted for comparison, and materials inside the dashed rectangle are expected to be more active and H_2O_2 selective than $PtHg_4$ (x $\leq$ 0.10, y $\leq$ 0.7).

ture using *GASpy*,[25] resulting in total 76,346 sites. Since 229,038 DFT jobs (76,346 × 3 considering bare, O* and OOH* adsorbed surfaces) are computationally too intensive, we reduced the number of structures based on the active motifs of interest, which are expected to selectively destabilize O* (Figure 3A).

To effectively reduce the number of DFT calculations, we considered multiple criteria. Since all 231 materials at this stage consist of bimetallic combinations of active and inactive
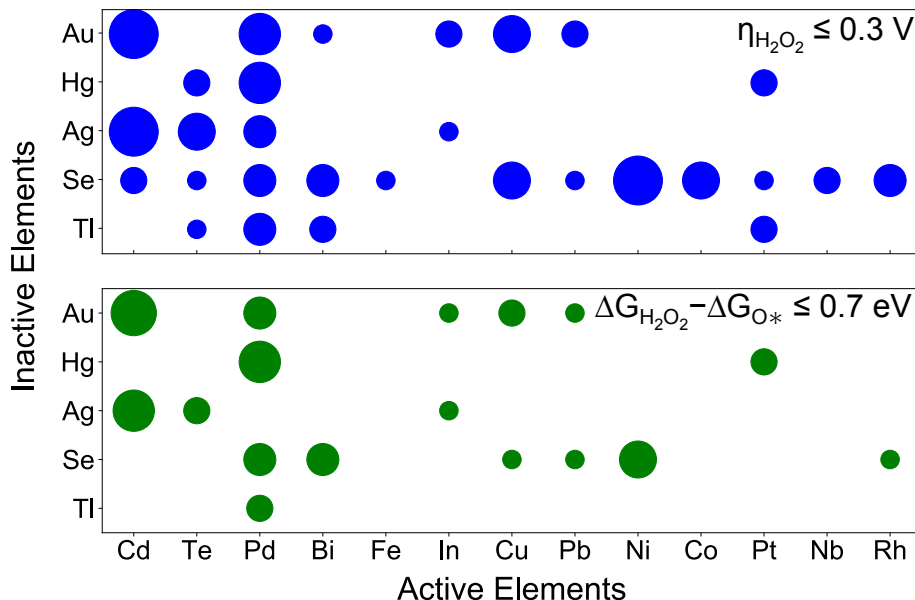
Figure 4: Bubble sizes representing the number of unique MPIDs consisting of combinations of active and inactive elements for high activity ($\eta_{H_2O_2} \leq 0.3$ V, upper plot) or selectivity ($\Delta G_{H_2O_2} - \Delta G_{O*} \leq 0.7$ eV, lower plot). Larger bubbles indicate more materials.

elements toward O-species, it is reasonable to assume that reaction intermediates (O* and OOH*) preferentially interact with more active elements at the top site, which reduced the number of sites from 76,346 to 12,514 (top site binding) to 4,804 (top site binding at active elements). We then categorized structures based on $CN_{inactive}$, defined as the number of the first nearest neighbor inactive elements surrounding the active elements (Figure 3A and 3B). Example structures of various $CN_{inactive}$ are presented in Figure S3.

Analysis

We first performed total 3,450 DFT calculations (1725 bare surfaces and 1725 OOH* adsorbed surfaces with $4 \leq CN_{inactive} \leq 9$) first to calculate ΔG_{OOH*}. We chose to consider $CN_{inactive}$ up to 4, since at least four inactive atoms are required to isolate the binding sites. 414 surfaces were found to be active with $\eta_{H_2O_2} \leq 0.3$ V (Figure 3C), where their ΔG_{O*} were subsequently calculated to evaluate H_2O_2 selectivity. In Figure 3D, we plotted 2e ORR activity, selectivity and acid-stability simultaneously, and we found 16 materials and 44 surfaces

that are expected to outperform $PtHg_4$ in terms of the catalytic activity and H_2O_2 selectivity (Table S3). We counted the number of unique materials (MPIDs) that are predicted to be active (upper plot in Figure 4) or selective (lower plot in Figure 4), and plotted histograms of active and inactive elements as bubbles to identify elements for high catalytic activity and selectivity that will be helpful for experimental validations in the future. Furthermore, detailed statistics of $\eta_{H_2O_2}$ are show in Figure S4. Se and Au elements were found to play an important role in fine-tuning ΔG_{OOH*} in combination with various active elements to minimize $\eta_{H_2O_2}$. Pd active sites in combination with all considered inactive elements achieved high catalytic activity. Further, many of Pd active sites were observed to be highly selective as well. In addition, we note that many structures of Pd-Au, Ni-Se, Cd-Au and Cd-Ag combinations were found to be promising candidates for experimental validations.

In Figure 5, we present examples of active and selective surfaces found from the active motif screening, and decompose the ensemble and the ligand effects originated from the change of binding site and local environment of the active site, respectively. A change of O* binding site from hollow to top (from B to C in Figure 5) weakened ΔG_{O*} by 1.38 eV, and shifted the point from $O_{hollow}*-OOH_{top}*$ scaling (green) to $O_{top}*-OOH_{top}*$ (orange). On the other hand, the ligand effects (from C to D/E) for $PdAu_3$ (0.16 eV) and Pd_7Se_4 (0.63 eV) were not as significant as the ensemble effect. We note that both $PdAu_3$ and Pd_7Se_4 are positioned at the scaling line of top site bindings obtained from the metal [111] surfaces, indicating that the ensemble effect significantly destabilized O* binding resulting in the transition to other scaling relation, and the ligand effect fine-tuned the ΔG_{OOH*}, shifting along the scaling relation.

We listed promising candidates predicted to be more active, selective and acid-stable than $PtHg_4$, where they were categorized with respect to the acid-stability (Table S4). In most cases, materials included noble metals such as Pd, Au, Pt and Rh. This is mainly because noble metals help to improve the acid-stabilities of the materials, where the effect of noble and non-noble elements on the acid-stabilities were visualized in our previous work.[32] Indeed,
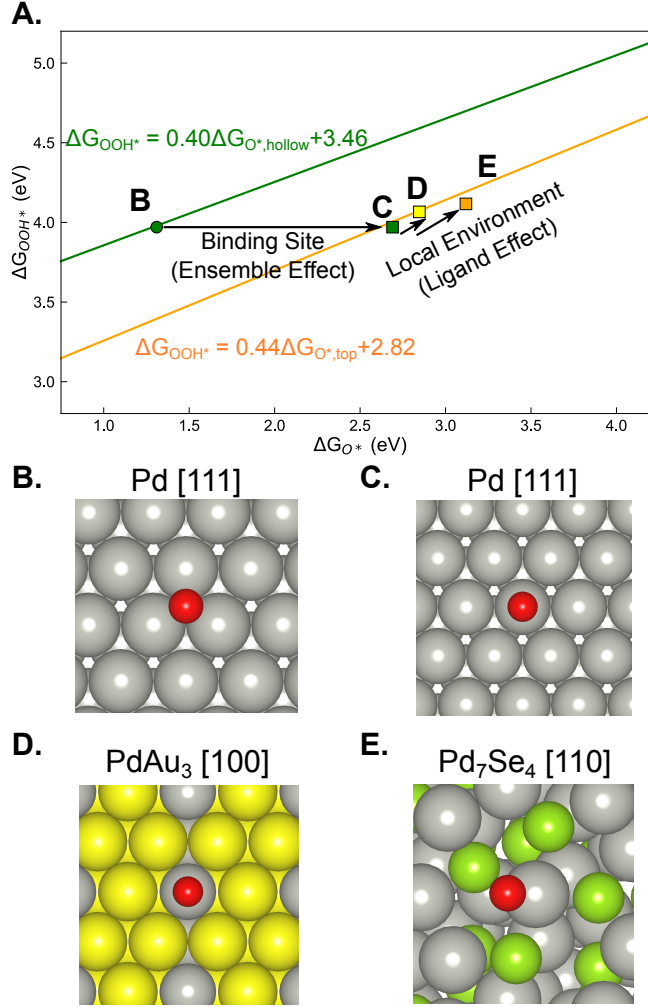
Figure 5: (A) The scaling relations between ΔG_{OOH*} and ΔG_{O*} from Figure 1B. Green and orange lines indicate hollow and top site O* binding, respectively. (B to E) Visual representations of example surfaces corresponding to the labels in Figure 5A. Color codes in atomic structures: Pd (grey), Au (yellow), Se (green) O (red).

materials consisting of non-noble metal combinations demonstrated worse acid-stability as in $CuSe_2$ and $NiSe_2$ although other catalytic properties were satisfactory. $PdAu_3$, Pd_7Se_4 and $CuAu_3$ were found to satisfy all conditions to outperform $PtHg_4$ in acid, and we note that some of them were already synthesized and tested for the 2e ORR.[33,34] Although we have focused on the acid-condition in this work, we note that the same analysis can be done using neutral-stability and base-stability to suggest promising candidates in different environments. For example, $CuSe_2$ is expected to be unstable under the acidic condition ($\Delta G_{Pourbaix}$=0.51 eV/atom), while it showed better stability under the neutral condition
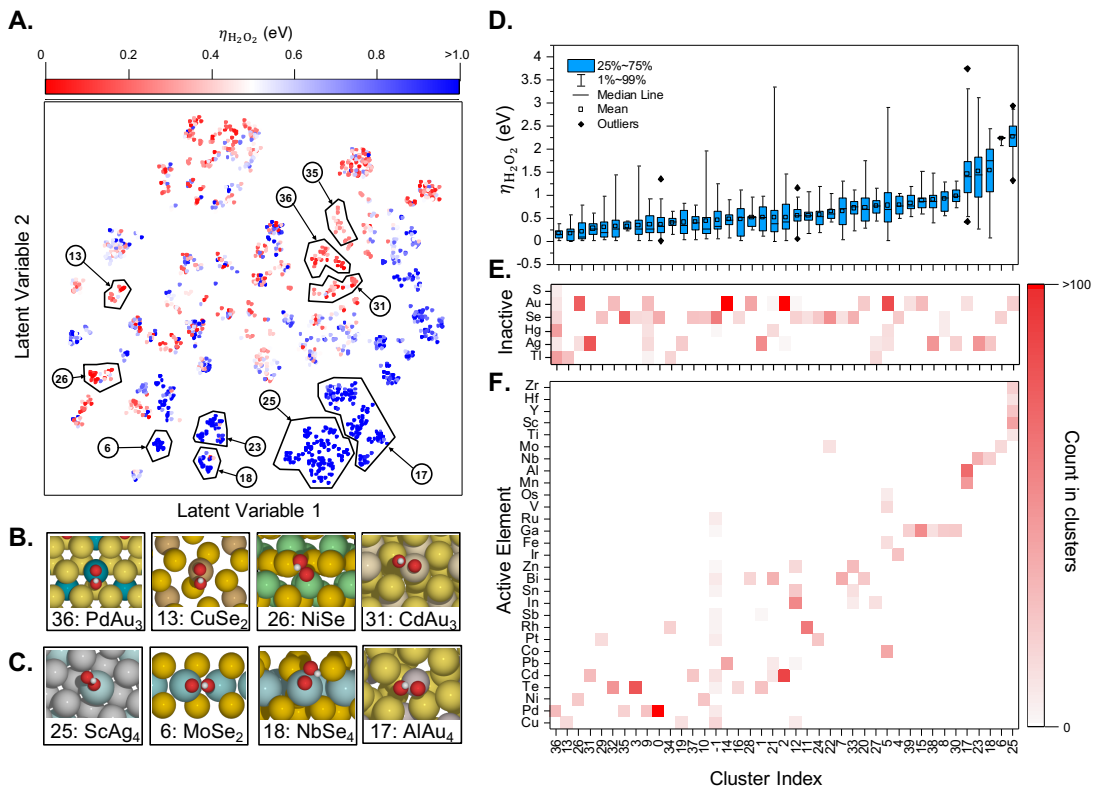
Figure 6: All surfaces considered in this work of which $\eta_{H_2O_2}$ were evaluated. (A) Two-dimensional latent space visualized by UMAP.[35] Location in the latent space represents similarities in active motifs. Several representative cluster indices categorized by DBSCAN[36] are highlighted. (B and C) Example atomic structures of catalytically (B) active and (C) inactive clusters in terms of $\eta_{H_2O_2}$. (D to F) Cluster characterization with (D) box plot of $\eta_{H_2O_2}$ distribution and occurrence heatmaps of (E) inactive and (F) active elements in each cluster.

($\Delta G_{\text{Pourbaix}}$=0.20 eV/atom).

Strategy Towards an Efficient High-Throughput Screening

We used uniform manifold approximation and projection (UMAP)[35] to reduce non-linear dimension of fingerprints. To generate fingerprints consisting of mixed-type of data (categorical: active and inactive elements for binding site and neighboring sites, numerical: OH binding energies of single atom alloys (Table S1), coordination numbers, and electrochemical stability), we transformed binding site and neighboring sites into fingerprints using an one-hot encoder and a multilabel binarizer, respectively, and attached their OH binding en-

15

ergies, coordination numbers, and electrochemical stability. An example of the fingerprint can be found in the Supporting Information (Figure S4). Bray–Curtis dissimilarity[37] was used to quantify a compositional dissimilarity between two different surfaces. Latent variables in the reduced space express representative information of surfaces in low dimension. Once the UMAP is learned, it is possible to visualize similarities of surfaces via fingerprint information which is obtained without DFT calculations (Figure 6A). To categorize surfaces with respect to their fingerprints, we used density-based spatial clustering of applications with noise (DBSCAN).[36] DBSCAN finds clusters throughout the latent space generated by UMAP, implying that UMAP-DBSCAN machine learning pipeline can be conducted before performing DFT calculations. The following results suggest that this approach could be used to reduce the number of DFT calculations.

After we plot the data on two-dimensional latent space and find clusters with similar fingerprints (Figure 6A), we analyzed statistics of $\eta_{H_2O_2}$ of each cluster. The box plot of catalytic activities (Figure 6D) and the occurrence heatmap of active elements (Figure 6F) illustrate a clear distinction of active and inactive surfaces. Especially, Figure 6F suggests that the catalytic activities are mainly affected by the identity of active elements. For example, we visualized OOH* adsorbed structures of active and inactive surfaces in Figure 6B and 6C, respectively, and the inactive surfaces are characterized by binding sites of early transition metals or p-block elements whose O-affinities were found to be very strong (Table S1). We also presented statistics of $\eta_{H_2O_2}$ with respect to active and inactive elements in Figure S5. Considering that UMAP-DBSCAN pipeline can successfully categorize similarly behaving surfaces, we can use this pipeline to reduce the amount of DFT calculations as follows: (1) we plot data in low-dimensional latent space using fingerprints, (2) we first calculate the $\eta_{H_2O_2}$ of subsets (e.g. core points via DBSCAN and a few other points nearby) of each cluster to find promising clusters and then (3) we perform full DFT calculations for chosen clusters. Following this procedure, we could avoid DFT calculations of several clusters of which the core points show poor catalytic activity (too high $\eta_{H_2O_2}$).

4. Conclusions

In this work, we systematically identify promising candidates for O_2 reduction to H_2O_2 through the active motif screening starting from Materials Project database. DFT calculations on the metal surfaces suggested the importance of the change in binding sites originated from the ensemble effect to tune the reaction pathway toward 2e ORR over 4e ORR. Based on this concept, we (1) evaluated their electrochemical stability to find stable materials under the reaction condition, (2) considered bimetallic combinations of active and inactive elements toward O-species, (3) generated all unique surfaces, and (4) categorized by the number of inactive elements surrounding the active ones, which allowed us to reduce the number of DFT calculations from 229,038 to 3,864. By considering multiple aspects of properties of catalysts, we found various candidates that are predicted to outperform the state-of-the-art intermetallic $PtHg_4$ and Pd_2Hg_5 catalysts. For future experimental attempts, we also listed active and inactive elements to achieve high activity and selectivity. We highlight the active motif screening is not limited to the ORR, but can also be applied to other catalytic reactions, where the ensemble effect helps to escape from the conventional scaling relation, resulting in significant enhancements in catalytic activity and selectivity. Finally, using DFT calculation results and the machine learning pipeline, we suggest an efficient strategy to accelerate high-throughput screening for catalyst discovery.

Acknowledgement

Grant of 2020.

Supporting Information Available

Free energy corrections for gases and adsorbates. Comparative analysis on Pt [111] and PtHg$_4$. Example structures of various CN$_{\text{inactive}}$. List of properties of promising candidates.

References

(1) Gamble, A. Ullmann's Encyclopedia of Industrial Chemistry. *The Charleston Advisor* **2019**, *20*, 46–50.

(2) Seh, Z. W.; Kibsgaard, J.; Dickens, C. F.; Chorkendorff, I.; Nørskov, J. K.; Jaramillo, T. F. Combining Theory and Experiment in Electrocatalysis: Insights into Materials Design. *Science* **2017**, *355*, eaad4998.

(3) Samanta, C. Direct Synthesis of Hydrogen Peroxide from Hydrogen and Oxygen: An Overview of Recent Developments in the Process. *Appl. Catal., A* **2008**, *350*, 133–149.

(4) Siahrostami, S.; Verdaguer-Casadevall, A.; Karamad, M.; Deiana, D.; Malacrida, P.; Wickman, B.; Escudero-Escribano, M.; Paoli, E. A.; Frydendal, R.; Hansen, T. W., et al. Enabling Direct H$_2$O$_2$ Production through Rational Electrocatalyst Design. *Nat. Mater.* **2013**, *12*, 1137.

(5) Verdaguer-Casadevall, A.; Deiana, D.; Karamad, M.; Siahrostami, S.; Malacrida, P.; Hansen, T. W.; Rossmeisl, J.; Chorkendorff, I.; Stephens, I. E. Trends in the Electrochemical Synthesis of H$_2$O$_2$: Enhancing Activity and Selectivity by Electrocatalytic Site Engineering. *Nano Lett.* **2014**, *14*, 1603–1608.

(6) Sa, Y. J.; Kim, J. H.; Joo, S. H. Active Edge-Site-Rich Carbon Nanocatalysts with En-

hanced Electron Transfer for Efficient Electrochemical Hydrogen Peroxide Production. *Angew. Chem. Int.* **2019**, *58*, 1100–1105.

(7) Lu, Z.; Chen, G.; Siahrostami, S.; Chen, Z.; Liu, K.; Xie, J.; Liao, L.; Wu, T.; Lin, D.; Liu, Y., et al. High-Efficiency Oxygen Reduction to Hydrogen Peroxide Catalysed by Oxidized Carbon Materials. *Nat. Catal.* **2018**, *1*, 156.

(8) Chen, S.; Chen, Z.; Siahrostami, S.; Kim, T. R.; Nordlund, D.; Sokaras, D.; Nowak, S.; To, J. W.; Higgins, D.; Sinclair, R., et al. Defective Carbon-Based Materials for the Electrochemical Synthesis of Hydrogen Peroxide. *ACS Sustain. Chem. Eng.* **2017**, *6*, 311–317.

(9) Chen, S.; Chen, Z.; Siahrostami, S.; Higgins, D.; Nordlund, D.; Sokaras, D.; Kim, T. R.; Liu, Y.; Yan, X.; Nilsson, E., et al. Designing Boron Nitride Islands in Carbon Materials for Efficient Electrochemical Synthesis of Hydrogen Peroxide. *J. Am. Chem. Soc.* **2018**, *140*, 7851–7859.

(10) Choi, C. H.; Choi, W. S.; Kasian, O.; Mechler, A. K.; Sougrati, M. T.; Brüller, S.; Strickland, K.; Jia, Q.; Mukerjee, S.; Mayrhofer, K. J., et al. Unraveling the Nature of Sites Active toward Hydrogen Peroxide Reduction in Fe-N-C Catalysts. *Angew. Chem. Int.* **2017**, *56*, 8809–8812.

(11) Jiang, K.; Back, S.; Akey, A. J.; Xia, C.; Hu, Y.; Liang, W.; Schaak, D.; Stavitski, E.; Nørskov, J. K.; Siahrostami, S., et al. Highly Selective Oxygen Reduction to Hydrogen Peroxide on Transition Metal Single Atom Coordination. *Nat. Commun.* **2019**, *10*, 1–11.

(12) Shi, C.; Chan, K.; Yoo, J. S.; Nørskov, J. K. Barriers of Electrochemical CO_2 Reduction on Transition Metals. *Org. Process Res. Dev.* **2016**, *20*, 1424–1430.

(13) Abild-Pedersen, F.; Greeley, J.; Studt, F.; Rossmeisl, J.; Munter, T.; Moses, P. G.; Skulason, E.; Bligaard, T.; Nørskov, J. K. Scaling Properties of Adsorption Energies for

Hydrogen-Containing Molecules on Transition-Metal Surfaces. *Phys. Rev. Lett.* **2007**, *99*, 016105.

(14) Fernández, E. M.; Moses, P. G.; Toftelund, A.; Hansen, H. A.; Martínez, J. I.; Abild-Pedersen, F.; Kleis, J.; Hinnemann, B.; Rossmeisl, J.; Bligaard, T., et al. Scaling Relationships for Adsorption Energies on Transition Metal Oxide, Sulfide, and Nitride Surfaces. *Angew. Chem. Int.* **2008**, *47*, 4683–4686.

(15) Wang, S.; Petzold, V.; Tripkovic, V.; Kleis, J.; Howalt, J. G.; Skulason, E.; Fernandez, E.; Hvolbæk, B.; Jones, G.; Toftelund, A.; Björketun, M.; Studt, F.; Abild-Pedersen, F.; Rossmeisl, J.; Nørskov, J. K.; Bligaard, T. Universal Transition State Scaling Relations for (De) Hydrogenation over Transition Metals. *Phys. Chem. Chem. Phys.* **2011**, *13*, 20760–20765.

(16) Kulkarni, A.; Siahrostami, S.; Patel, A.; Nørskov, J. K. Understanding Catalytic Activity Trends in the Oxygen Reduction Reaction. *Chem. Rev.* **2018**, *118*, 2302–2312.

(17) Kresse, G., et al. G. Kresse and J. Furthmüller, Comput. Mater. Sci. 6, 15 (1996). *Comput. Mater. Sci.* **1996**, *6*, 15.

(18) Kresse, G.; Hafner, J. Ab Initio Molecular Dynamics for Open-Shell Transition Metals. *Phys. Rev. B* **1993**, *48*, 13115.

(19) Hammer, B.; Hansen, L. B.; Nørskov, J. K. Improved Adsorption Energetics within Density-Functional Theory using Revised Perdew-Burke-Ernzerhof Functionals. *Phys. Rev. B* **1999**, *59*, 7413.

(20) Kresse, G.; Joubert, D. From Ultrasoft Pseudopotentials to the Projector Augmented-Wave Method. *Phys. Rev. B* **1999**, *59*, 1758.

(21) Larsen, A. H.; Mortensen, J. J.; Blomqvist, J.; Castelli, I. E.; Christensen, R.; Dułak, M.; Friis, J.; Groves, M. N.; Hammer, B.; Hargus, C.; Hermes, E. D.; Jen-

nings, P. C.; Jensen, P. B.; Kermode, J.; Kitchin, J. R.; Kolsbjerg, E. L.; Kubal, J.; Kaasbjerg, K.; Lysgaard, S.; Maronsson, J. B.; Maxson, T.; Olsen, T.; Pastewka, L.; Peterson, A.; Rostgaard, C.; Schiøtz, J.; Schütt, O.; Strange, M.; Thygesen, K. S.; Vegge, T.; Vilhelmsen, L.; Walter, M.; Zeng, Z.; Jacobsen, K. W. The Atomic Simulation Environment—a Python Library for Working with Atoms. *J. Condens. Matter Phys.* **2017**, *29*, 273002.

(22) Tripković, V.; Skúlason, E.; Siahrostami, S.; Nørskov, J. K.; Rossmeisl, J. The Oxygen Reduction Reaction Mechanism on Pt (111) from Density Functional Theory Calculations. *Electrochim. Acta* **2010**, *55*, 7975–7981.

(23) Nørskov, J. K.; Rossmeisl, J.; Logadottir, A.; Lindqvist, L.; Kitchin, J. R.; Bligaard, T.; Jonsson, H. Origin of the Overpotential for Oxygen Reduction at a Fuel-cell Cathode. *J. Phys. Chem. B* **2004**, *108*, 17886–17892.

(24) Hammer, B.; Norskov, J. K. Why Gold is the Noblest of All the Metals. *Nature* **1995**, *376*, 238–240.

(25) Tran, K.; Ulissi, Z. W. Active Learning across Intermetallics to Guide Discovery of Electrocatalysts for CO_2 Reduction and H_2 Evolution. *Nat. Catal.* **2018**, *1*, 696–703.

(26) Back, S.; Yoon, J.; Tian, N.; Zhong, W.; Tran, K.; Ulissi, Z. W. Convolutional Neural Network of Atomic Surface Structures to Predict Binding Energies for High-Throughput Screening of Catalysts. *J. Phys. Chem. Lett.* **2019**, *10*, 4401–4408.

(27) Gu, G. H.; Noh, J.; Kim, S.; Back, S.; Ulissi, Z. W.; Jung, Y. Practical Deep-Learning Representation for Fast Heterogeneous Catalyst Screening. *J. Phys. Chem. Lett.* **2020**,

(28) automatminer: An autoML tool for materials. 2019; https://github.com/hackingmaterials/automatminer.

(29) Jain, A.; Ong, S. P.; Hautier, G.; Chen, W.; Richards, W. D.; Dacek, S.; Cholia, S.; Gunter, D.; Skinner, D.; Ceder, G., et al. Commentary: The Materials Project: A Materials Genome Approach to Accelerating Materials Innovation. *APL Mater.* **2013**, *1*, 011002.

(30) Back, S.; Tran, K.; Ulissi, Z. W. Discovery of Acid-Stable Oxygen Evolution Catalysts: High-throughput Computational Screening of Equimolar Bimetallic Oxides. *ACS Appl. Mater. Interfaces* **2020**, *12*, 38256–38265.

(31) Wang, Z.; Zheng, Y.-R.; Chorkendorff, I.; Norskov, J. K. Acid-Stable Oxides for Oxygen Electrocatalysis. *ACS Energy Lett.* **2020**, *5*, 2905–2908.

(32) Back, S.; Na, J.; Tran, K.; Ulissi, Z. In silico Discovery of Active, Stable, CO-Tolerant and Cost-Effective Electrocatalysts for Hydrogen Evolution and Oxidation. *Phys. Chem. Chem. Phys.* **2020**, *22*, 19454–19458.

(33) Kurnatowski, M.; Bortz, M.; Klein, P.; Kintzel, B.; Cremers, C. Quantitative Kinetic Analysis of a $PdAu_3$ Alloy Catalyst for Oxygen Electro-Reduction. *J. Electrochem.* **2017**, *164*, 1072.

(34) Kukunuri, S.; Naik, K.; Sampath, S. Effects of Composition and Nanostructuring of Palladium Selenide Phases, Pd_4Se, Pd_7Se_4 and $Pd_{17}Se_{15}$, on ORR Activity and Their Use in Mg–Air Batteries. *J. Mater. Chem. A* **2017**, *5*, 4660–4670.

(35) McInnes, L.; Healy, J.; Melville, J. UMAP: Uniform Manifold Approximation and Projection for Dimension Reduction. *Preprint at https://arxiv.org/abs/1802.03426 (2018)*

(36) Ester, M.; Kriegel, H.-P.; Sander, J.; Xu, X. A Density-based Algorithm for Discovering Clusters in Large Spatial Databases with Noise. KDD. 1996; pp 226–231.

(37) Bray, J. R.; Curtis, J. T. An Ordination of the Upland Forest Communities of Southern Wisconsin. *Ecol. Monogr.* **1957**, *27*, 326–349.

Graphical TOC Entry

Selective Electrochemical O$_2$ Reduction

Active Motif Screening